Parity-Violating Electron Scattering and the Electric and Magnetic Strange Form Factors of the Nucleon

D.S. Armstrong[1] and R.D. McKeown[2]

[1]Department of Physics, College of William and Mary, Williamsburg, Virginia 23187

[2]Thomas Jefferson National Accelerator Facility, Newport News, Virginia 23606; Department of Physics, College of William and Mary, Williamsburg, Virginia 23187

Annu. Rev. Nucl. Part. Sci. 2012. 62:337–59

The *Annual Review of Nuclear and Particle Science* is online at nucl.annualreviews.org

This article's doi:
10.1146/annurev-nucl-102010-130419

0163-8998/12/1123-0337$20.00

Keywords

neutral current, lepton scattering, electromagnetic form factors, strange form factors

Abstract

Measurements of the neutral weak-vector form factors of the nucleon provide unique access to the strange quark content of the nucleon. These form factors can be studied by using parity-violating electron scattering. A comprehensive program of experiments has been performed at three accelerator laboratories to determine the role of strange quarks in the electromagnetic form factors of the nucleon. This article reviews the remarkable technical progress associated with this program, describes the various methods used in the different experiments, and summarizes the physics results along with recent theoretical calculations.

Contents

1. INTRODUCTION

Since the initial development of quantum chromodynamics (QCD) in the 1970s, it has been known that the internal structure of the nucleon is due to the presence of quarks, gluons, and a sea of quark-antiquark pairs. Although the electric charge of the nucleon is due to the valence quarks (as in the early quark models proposed by Gell-Mann and Zweig), in QCD the gluons are critical to quark confinement, generating 98% of the nucleon mass in the process. The results of polarized deep-inelastic scattering experiments in the 1980s and 1990s indicated that, contrary to theoretical expectations, the spin of the nucleon does not arise from the spins of the quarks. As a result, the role of the gluons and the quark-antiquark pairs in the static properties of the nucleon became a subject of great interest. Although the gluons are responsible for dramatic effects such as confinement and nucleon mass, the effects of the quark-antiquark pairs (necessarily generated by the gluons in QCD and therefore nonzero) are more difficult to ascertain. One can think of such pair excitations as the QCD analog of the famous Lamb shift in atomic physics.

The strange quark–antiquark pairs are of particular interest because there are no valence strange quarks in the nucleon and any process sensitive to strange quarks would necessarily be related to the sea. In 1988, Kaplan & Manohar (1) proposed the study of strange quark–antiquark pairs by measurements of neutral weak current matrix elements, perhaps in neutrino scattering experiments. In 1989, McKeown (2) and Beck (3) proposed that parity-violating electron scattering would offer a very effective method to study these matrix elements, generating significant interest and many new experimental proposals. Over the subsequent two decades, a great deal of experimental and theoretical effort created a now-definitive body of work that, for the first time, substantially constrains the contribution of strange quark–antiquark pairs to the elastic electroweak form factors of the nucleon.

2. STRANGE QUARKS IN THE NUCLEON

The most direct evidence for the existence of quarks and antiquarks in the nucleon is obtained from deep-inelastic lepton scattering. In this process, a high-momentum virtual photon interacts

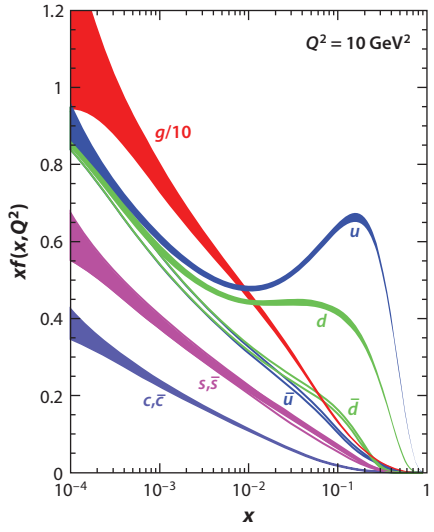

Figure 1

The results of a global fit (4) for the quark, antiquark, and gluon parton distribution functions (PDFs), as a function of the momentum fraction x, at $Q^2 = 10$ GeV^2. Note that the PDFs $f(x)$ are multiplied by x to suppress the large rise at low x in the plot and that the gluon distribution is divided by 10 for display purposes. Reprinted from Reference 4 with permission.

with the fundamental charges in the nucleon (quarks and antiquarks). Through the study of lepton-proton and lepton-neutron scattering, and by using charge symmetry (with approximate treatment of charge symmetry–breaking effects), one can extract information related to the probability distributions for up, down, and sea quarks. These distributions, known as parton distribution functions (PDFs), are defined as a function of momentum fraction in the nucleon, x ($0 < x < 1$), and are denoted $q(x)$ and $\bar{q}(x)$, where $q = u,\ d,\ c,\ s,\ t,$ or b for the quark flavors. In addition, the production of like-sign dimuon pairs in deep-inelastic charged-current neutrino scattering provides information about the strange quark distribution. Another important ingredient in the flavor decomposition of the sea quarks is provided by Drell–Yan experimental data, in which an incident quark (in the projectile nucleon) annihilates on an antiquark (in the target nucleon) to produce a $\mu^+\mu^-$ pair. Recent Drell–Yan data on the proton and deuteron have been combined to indicate a startling excess of $\bar{d}(x)/\bar{u}(x)$. Finally, the evolution of the quark and antiquark PDFs as a function of Q^2 provides information about the gluon PDF $g(x)$. **Figure 1** shows the results of the PDFs obtained in a recent global fit to deep-inelastic scattering and Drell–Yan data.

The general features of the PDFs shown in **Figure 1** are qualitatively well understood. The dominance of u and d at high x ($x > 0.1$) indicates the valence nature of these quark flavors (three valence quarks, each with an average x of approximately 1/3). The dramatic rise of $g(x)$ at low x is associated with the "splitting" of partons at lower x, such as $q(x) \rightarrow q(y) + g(x - y)$. The sea quarks arise from $\bar{q}q$ pair production by gluons via $g(x) \rightarrow q(y) + \bar{q}(x - y)$. Thus, one can infer that the gluons dominate the dynamics at low x and that the presence of the sea quarks is a secondary feature of the presence of the large number density of gluons.

However, there is a very interesting and important effect at intermediate x ($0.01 < x < 0.1$), where (due to the Drell–Yan data discussed above) one finds a substantial excess of $\bar{d}(x)$ relative to $\bar{u}(x)$. Clearly, the process $g \rightarrow \bar{q}q$ produces $\bar{u} = \bar{d}$ (except for small effects due to $m_u \neq m_d$). The $\bar{d}(x)/\bar{u}(x)$ excess must then be attributed to nonperturbative processes. For example, the

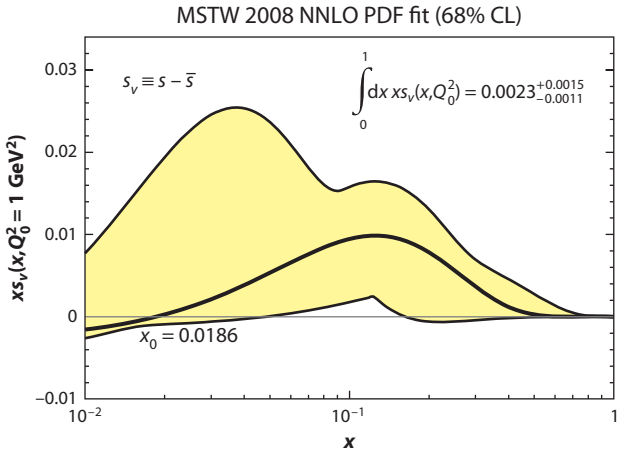

Figure 2

The results of the recent global fit (4) for the difference $s(x) - \bar{s}(x)$. Abbreviations: NNLO, next-to-next-to-leading order; PDF, parton distribution function. Reprinted from Reference 4 with permission.

fluctuation of a proton into a neutron and π^+ contains a $\bar{d}$ component, and there is no symmetric analog process to produce $\bar{u}$. (Note that $p \rightarrow p\pi^0$ produces equal numbers of $\bar{u}$ and $\bar{d}$.) In addition, one would expect the $\bar{d}$ excess from this process to occur at the value $x \sim m_\pi/(2m_N)$, in agreement with the experimental data. Thus, the observed excess of $\bar{d}(x)/\bar{u}(x)$ strongly indicates the presence of fluctuations into $N\pi$ pairs in the nucleon. Of course, many models of the nucleon (such as the so-called cloudy bag models) include such configurations in an attempt to capture the physics associated with other observables (such as the anomalous magnetic moments).

Thus, one is naturally led to consider the possible role of similar fluctuations, such as $p \rightarrow K^+\Lambda$. Clearly, such configurations have a lower probability than that of $N\pi$ fluctuations due to the higher masses of the Λ and K^+, but finite observable effects should certainly result from them. Such configurations would lead to radially separated distributions of $\bar{s}$ and s quarks due to the tendency of the K^+ to occupy larger radial distances from the center of mass of the ΛK^+. The spatial separation of s and $\bar{s}$ would have several implications: (*a*) an $\bar{s}s$ contribution to the nucleon magnetic moment, as well as other electroweak form factors; (*b*) an $\bar{s}s$ contribution to the nucleon axial charge, which would affect the value of Σ associated with the helicity carried by quarks; (*c*) an $\bar{s}s$ contribution to the mass of the nucleon; and (*d*) a difference between the PDFs $s(x)$ and $\bar{s}(x)$.

Items *a*, *b*, and *c* are low-Q^2 or static properties of the nucleon. Thus, they represent a change in the nucleon static properties that is analogous to the change in atomic properties (e.g., the Lamb shift) due to vacuum polarization in QED. Item *d* is an effect that is analogous to the $\bar{d}(x)/\bar{u}(x)$ excess observed in the Drell–Yan process. In principle, items *a* and *d* can be established in a model-independent fashion, whereas items *b* and *c* generally require a model-dependent analysis or assumptions about nonperturbative QCD effects.

At present, although there have been many hints of effects associated with items *b* and *c*, there is no unassailable demonstration that the evidence arises from strange quark effects. For item *d*, there is only a hint in the latest global PDF fit, MSTW08 (**Figure 2**) (4). The remainder of this review focuses on the theoretical framework, experimental techniques, and experimental results associated with the studies of the $\bar{s}s$ contribution to the nucleon magnetic moment, as well as other electroweak form factors (item *a*).

3. NEUTRAL WEAK FORM FACTORS

The elastic scattering of nucleons via the neutral weak current can be described by two vector form factors, F_1^Z and F_2^Z, and an axial vector form factor, G^Z. These form factors are functions of the invariant momentum transfer, Q^2. Like the electromagnetic interaction, the neutral weak interaction with a nucleon involves coupling to the quarks (and antiquarks) because the gluons have no electroweak interaction. In general, we can write any of the elastic electroweak form factors in terms of the quark flavors. For example, the electromagnetic form factors are given by

$$F_1^\gamma = \frac{2}{3}F_1^u - \frac{1}{3}F_1^d - \frac{1}{3}F_1^s \quad 1.$$

and

$$F_2^\gamma = \frac{2}{3}F_2^u - \frac{1}{3}F_2^d - \frac{1}{3}F_2^s, \quad 2.$$

where u, d, and s refer to the up, down, and strange quarks, respectively. Note that we ignore charm and heavier quarks because studies show that they can be safely neglected. The neutral weak form factors may be also written in terms of the individual quark flavor components,

$$F_{1,2}^Z = \left(1 - \frac{8}{3}\sin^2\theta_W\right)F_{1,2}^u + \left(-1 + \frac{4}{3}\sin^2\theta_W\right)\left(F_{1,2}^d + F_{1,2}^s\right) \quad 3.$$

and

$$G_A^Z = -G_A^u + G_A^d + G_A^s, \quad 4.$$

where θ_W is the weak mixing angle. The value of θ_W is, in principle, precisely determined from other experiments (5), although one must consider the renormalization scheme and radiative corrections.

For the vector form factors, one often prefers to use the Sachs form factors

$$\begin{aligned} G_E^{\gamma,Z} &= F_1^{\gamma,Z} - \tau F_2^{\gamma,Z}, \\ G_M^{\gamma,Z} &= F_1^{\gamma,Z} + F_2^{\gamma,Z}, \end{aligned} \quad 5.$$

where $\tau \equiv Q^2/4M^2$. In the static limit, the electromagnetic form factors then reduce to the charge and magnetic moment: $G_E^\gamma(Q^2 = 0) = Q$ and $G_M^\gamma(Q^2 = 0) = \mu$. Another useful quantity is the charge radius,

$$\langle r^2\rangle = -6\frac{dG_E(Q^2)}{dQ^2}\bigg|_{Q^2=0}. \quad 6.$$

Assuming isospin symmetry, additional relations among the form factors are obtained by use of the fact that the transformation of proton to neutron ($p \to n$) is equivalent to changing u to d and vice versa ($u \leftrightarrow d$). For example, the proton and neutron axial form factors are then related to the quark components (defined for the proton) by

$$G_A^{Z,p} = -G_A^u + G_A^d + G_A^s \quad 7.$$

and

$$G_A^{Z,n} = -G_A^d + G_A^u + G_A^s. \quad 8.$$

One can then isolate the strange axial form factor by

$$G_A^s = \frac{(G_A^{Z,p} + G_A^{Z,n})}{2}. \quad 9.$$

In principle, Equation 9 would be a way to access the matrix element $G_A^s(Q^2 = 0) = \langle\bar{s}\gamma^\mu\gamma_5 s\rangle S_\mu$, where S is the nucleon spin four-vector. Again, in practice one must consider radiative corrections

and, for this axial form factor, the contribution of anapole effects (as discussed in Section 3.2, below). The theoretical uncertainties associated with these corrections render measurement of the strange contribution Δs problematic in parity-violating electron scattering.

For the vector form factors, the use of isospin symmetry yields the important relation

$$G_{E,M}^{Z,p} = (1 - 4\sin^2\theta_W)G_{E,M}^{\gamma,p} - G_{E,M}^{\gamma,n} - G_{E,M}^{s}, \qquad 10.$$

which illustrates how measurements of the electromagnetic form factors for the proton and neutron, combined with measurements of the corresponding $G^{Z,p}$, can provide access to the strange vector form factors. In this case, as discussed in Section 3.1, the radiative corrections are manageable, and parity-violating electron scattering is a very useful tool for the study of strange vector form factors. In the static limit, one has the particularly interesting quantity $\mu_s \equiv G_M^s(Q^2 = 0)$, which is known as the strange magnetic moment. Because the net strangeness in the nucleon is zero, $G_E^s(Q^2 = 0) = 0$. However, the mean squared strangeness radius, $r_s^2 \equiv -6(dG_E/dQ^2)(Q^2 = 0)$, is a static property that generally can be nonzero.

Over the past two decades, numerous theoretical papers have reported predictions for strange vector form factors. Most of these papers involve models of nucleon structure that, although well motivated, involve many uncertainties related to the expected accuracy of the predictions. A good review of the model calculations can be found in Reference 6. Many of the models predict values for μ_s, and the results generally range from -0.5 to 0.3 nm; there is a strong preference for negative values. The predicted values for r_s also cover a substantial range: $-0.25 < r_s < 0.4$ fm.

Over the past few years, calculations based on input from lattice QCD methods have become available. The challenge associated with lattice calculations involves the evaluation of so-called disconnected insertions, in which the vector current couples to a quark loop that does not involve the valence quarks. (Because there are no valence strange quarks, these are the amplitudes that are relevant to the strange form factors.) In one approach (7), the baryon octet matrix elements are written with connected and disconnected insertions in separate terms. Linear combinations of the baryon magnetic moments are used, along with the assumption of charge symmetry, to obtain expressions involving the baryon magnetic moments and the ratios of amplitudes to be evaluated using lattice calculations. The authors (7) claim that the ratios are reliably determined from lattice calculations, and this method yields the prediction $\mu_s = -0.046 \pm 0.019$ nm; the uncertainty is estimated from the lattice statistical precision. A similar approach (8) was then used to compute the strange radius, $r_s^2 = 0.021 \pm 0.063$ fm^2, where the uncertainty arises predominantly from the poor experimental information on baryon charge radii.

More recently, a more direct approach (9) using lattice methods was employed. By using a full QCD calculation with $N_f = 2 + 1$ clover fermion configurations, the authors obtained the result $\mu_s = -0.017 \pm 0.025 \pm 0.07$ nm, where the first uncertainty is statistical and the second is due to uncertainties in Q^2 and chiral extrapolations. This result is in remarkable agreement with the more phenomenological result (7).

3.1. Radiative Corrections

To extract the contributions of strange form factors G^s from measurements of electroweak form factors, one must include the effects of $\mathcal{O}(\alpha)$ electroweak radiative corrections. These radiative effects typically arise from $\gamma - Z$ box diagrams or loop effects. It is common to express these $\mathcal{O}(\alpha)$ corrections as ratios $R_{V,A}$ (for vector V and axial vector A), which are fractions of the corresponding tree-level amplitudes. R_V^p, R_V^n, and $R_V^{(0)}$ denote the ratios for vector proton, neutron, and $SU(3)$-singlet amplitudes, respectively. In principle, their values can be obtained by use of the Standard Model predictions for the effective electron-quark couplings, C_{1q}, given in Reference 5. However,

these C_{1q} do not include perturbative QCD contributions or coherent strong-interaction effects in the radiative corrections associated with elastic scattering from a nucleon. Reference 10 gives a recent analysis of these effects; Reference 11 updates this analysis and includes an improved treatment of strong-interaction contributions to the running of the weak mixing angle in the $\overline{MS}$ renormalization scheme from its value at the Z pole. The results from this analysis are

$$R_V^p = -0.0520, \quad 11.$$

$$R_V^n = -0.0123, \quad 12.$$

and

$$R_V^{(0)} = -0.0123. \quad 13.$$

The theoretical uncertainties in R_V^n and $R_V^{(0)}$ are less than 1%, whereas the theoretical uncertainty in $(1 - 4\sin^2\theta_W)(1 + R_V^p)$ is ± 0.0008 (11), or slightly more than 1%. [Because this error receives roughly equal contributions from the uncertainty in $\sin^2\hat{\theta}_W(M_Z)$ as determined at the Z pole and from the $\mathcal{O}(\alpha)$ $Z\gamma$ box graph corrections, it is not appropriate to quote an uncertainty in R_V^p alone.] For the range of Q^2 associated with the experiments discussed in this review, R_V has a negligible impact on the Q^2 dependence of A_{PV}^p and is taken to be constant. We adopt the conventional $\overline{MS}$ renormalization scheme so that $\sin^2\hat{\theta}_W$ is evaluated as $\sin^2\hat{\theta}_W(M_Z) = 0.23116 \pm 0.00013$ (5).

3.2. Axial Form Factor Corrections

For the axial form factor, it is useful to employ the notation G_A^e to differentiate the quantity relevant to parity-violating electron scattering from other axial form factors (i.e., charged-current processes and neutrino scattering). At lowest order, this axial form factor is the same as G_A as measured in charged-current processes [$G_A(Q^2 = 0) = -1.2701 \pm 0.0025$] (5). However, the presence of strange quarks (i.e., the contribution Δs) and radiative effects must be included and can be expressed as

$$G_A^e(Q^2) = G_D(Q^2) \times \left[G_A\left(1 + R_A^{T=1}\right) + \frac{3F - D}{2} R_A^{T=0} + \Delta s\left(1 + R_A^{(0)}\right) \right], \quad 14.$$

where

$$G_D(Q^2) = \frac{1}{(1 + Q^2/M_A^2)^2} \quad 15.$$

parameterizes the Q^2 dependence with a dipole form with the squared axial mass $M_A^2 = 1.00 \pm 0.04$ GeV^2 (12). F and D are the octet baryon β-decay parameters, which are determined from neutron and hyperon β decays under the assumption of $SU(3)$ flavor symmetry [$3F - D = 0.58 \pm 0.12$ (13)]. $\Delta s = -0.07 \pm 0.06$ (14) is the strange quark contribution to nucleon spin obtained from inclusive polarized deep-inelastic lepton-nucleon scattering.

The ratios $R_A^{T=1}$, $R_A^{T=0}$, and $R_A^{(0)}$ characterize the effect of electroweak radiative corrections to the isovector, isoscalar, and $SU(3)$ singlet components of the axial form factor. These quantities are traditionally divided into "one-quark" and "many-quark" contributions. The one-quark contributions correspond to the renormalization of the effective vector electron–axial vector quark couplings, C_{2q}, and their values can be obtained from the Standard Model predictions for these couplings, given in Reference 5. The many-quark contributions include the so-called anapole effects, as well as coherent strong-interaction contributions to the radiative corrections. As originally pointed out by Zeldovich (15), an object can have a parity-violating coupling to the electromagnetic field that arises from internal weak interactions, which is known as an anapole moment. In

contrast to the vector corrections, R_V, the relative importance of many-quark effects in the axial corrections R_A can be quite pronounced. The many-quark effects can be addressed through the use of chiral perturbation theory, and a comprehensive analysis of the anapole contributions to $R_A^{T=1}$ and $R_A^{T=0}$ has been carried out to chiral order p^3 (16). The total axial corrections, updated for the present value of the weak mixing angle, are

$$R_A^{T=1} = -0.258 \pm 0.34, \quad 16.$$

$$R_A^{T=0} = -0.239 \pm 0.20, \quad 17.$$

and

$$R_A^{(0)} = -0.55 \pm 0.55. \quad 18.$$

4. PARITY-VIOLATING ELECTRON SCATTERING

4.1. Theory

The scattering of an electron from a hadronic target involves the dominant electromagnetic amplitude due to photon exchange, $\mathcal{M}_\gamma$, and the much smaller (at low momentum transfer, $Q^2 \ll M_Z^2$) neutral weak amplitude due to Z exchange, $\mathcal{M}_Z$ (**Figure 3**). The scattering cross section is related to the squared modulus of the sum of these amplitudes, $|\mathcal{M}_\gamma + \mathcal{M}_Z|^2$. Parity-violating observables arise from the fact that the weak amplitude involves both vector and axial vector currents, which leads to pseudoscalar quantities. The incident electron helicity, $\hat{s} \cdot \hat{k}$, is a pseudoscalar quantity, so the helicity dependence of the cross section violates parity symmetry and must involve the weak amplitude. To lowest order, one expects the difference between positive helicity and negative helicity cross sections to depend on the product $d\sigma_R - d\sigma_L \propto \mathrm{Re}[\mathcal{M}_\gamma \mathcal{M}_Z^{V\,A}]$, where $\mathcal{M}_Z^{V\,A}$ is the weak amplitude associated with the product of the vector and axial vector currents. The helicity-independent cross section is simply due to the dominant photon-exchange amplitude $d\sigma_R + d\sigma_L \propto |\mathcal{M}_\gamma|^2$. Thus, the parity-violating helicity-dependent asymmetry has the following structure:

$$A_{LR} \equiv \frac{d\sigma_R - d\sigma_L}{d\sigma_R + d\sigma_L} \quad 19.$$

$$\propto \frac{\mathrm{Re}[\mathcal{M}_\gamma \mathcal{M}_Z^{V\,A}]}{|\mathcal{M}_\gamma|^2}. \quad 20.$$

The squared electromagnetic amplitude must be proportional to $(e/Q^2)^4 = (4\pi\alpha/Q^2)^2$, whereas the product $\mathcal{M}_\gamma \mathcal{M}_Z^{V\,A}$ is proportional to $(e/Q^2)^2 G_F/\sqrt{2} = 4\pi\alpha G_F/\sqrt{2}Q^2$. (At low Q^2, the weak amplitude involves the Fermi coupling constant, $G_F = 1.16637 \times 10^{-5}$ GeV^{-2}.) Therefore, the

Figure 3

The amplitudes relevant to parity-violating electron scattering. The dominant parity-violating effects arise from the interference of these two amplitudes.

parity-violating asymmetry can be written as

$$A_{\rm LR} = -\frac{G_{\rm F} Q^2}{4\sqrt{2}\pi\alpha}\frac{\mathcal{N}}{\mathcal{D}}, \qquad 21.$$

in which the numerator $\mathcal{N}$ involves products of electromagnetic and weak form factors and the denominator $\mathcal{D}$ involves squares of electromagnetic form factors.

At lowest order, the expression for parity-violating electron-nucleon scattering in the laboratory frame of reference (where the initial nucleon is at rest) is given by

$$A_{\rm LR} \equiv \frac{d\sigma_{\rm R} - d\sigma_{\rm L}}{d\sigma_{\rm R} + d\sigma_{\rm L}} \qquad 22.$$

$$= \left[\frac{-G_{\rm F} Q^2}{4\sqrt{2}\pi\alpha}\right](A_E + A_M + A_A), \qquad 23.$$

where the three terms are

$$A_E = \frac{\varepsilon G_E^\gamma G_E^Z}{\epsilon (G_E^\gamma)^2 + \tau (G_M^\gamma)^2}, \qquad 24.$$

$$A_M = \frac{\tau G_E^\gamma G_M^Z}{\epsilon (G_E^\gamma)^2 + \tau (G_M^\gamma)^2}, \qquad 25.$$

and

$$A_A = \frac{-\epsilon'(1 - 4\sin^2\theta_W) G_M^\gamma G_A^e}{\epsilon (G_E^\gamma)^2 + \tau (G_M^\gamma)^2}, \qquad 26.$$

involving the kinematic variables

$$\begin{aligned} \tau &= \frac{Q^2}{4M_N^2}, \\ \epsilon &= \frac{1}{1 + 2(1+\tau)\tan^2\frac{\theta}{2}}, \\ \epsilon' &= \sqrt{\tau(1+\tau)(1-\epsilon^2)}, \end{aligned} \qquad 27.$$

which are functions of the momentum transfer $Q^2 = -q^2 > 0$ and the electron scattering angle θ. The different terms, A_E, A_M, and A_A, depend on the neutral weak form factors associated with the electric, magnetic, and axial couplings to the nucleon and so provide access to the strange form factors G_E^s, G_M^s, and G_A^s, respectively. At small scattering angles, $\theta \to 0$, one finds that $\epsilon \to 1$, $\tau \to 0$, and $\epsilon' \to 0$, so A_E becomes the dominant term. At backward angles, $\theta \to \pi$, $\epsilon \to 0$ and the asymmetry is dominated by the magnetic and axial asymmetries. Note also that the axial asymmetry is suppressed by the factor $(1 - 4\sin^2\theta_W)$, but the actual numerical value is quite sensitive to radiative and anapole effects. As a result, the dependence of $A_{\rm LR}$ on G_A^s is quite small, so one uses G_A^s as determined from spin-dependent deep-inelastic scattering. Thus, in the end, one can treat $A_{\rm LR}$ as a (linear) function of the vector strange form factors G_E^s and G_M^s.

By evaluating Equation 23 in terms of the vector strange form factors and by including radiative corrections, one can express the asymmetry as

$$A_{\rm LR} = A_{\rm nvs} + \eta_E G_E^s + \eta_M G_M^s, \qquad 28.$$

where $A_{\rm nvs}$ is the nonvector-strange asymmetry (independent of G_E^s and G_M^s) and both η_E and η_M are functions of kinematic quantities and nucleon electromagnetic form factors. For elastic scattering from the proton, one can measure the asymmetry at various scattering angles and fixed momentum transfer (by also varying the incident beam energy) to obtain values for different linear combinations of the strange vector form factors. This procedure (analogous to the

Rosenbluth separation for determining form factors from cross-section measurements) facilitates the determination of both G_E^s and G_M^s.

Another technique for performing experimental measurements of G_E^s involves elastic scattering from ^{4}He. The ^{4}He nucleus has spin $S = 0$ and isospin $I = 0$, so the magnetic and axial form factors vanish. The charge form factor for electromagnetic scattering from ^{4}He is proportional to the isoscalar combination $G_E^{\gamma,p} + G_E^{\gamma,n}$. Similarly, the neutral weak form factor is proportional to $G_E^{Z,p} + G_E^{Z,n}$. One can use Equation 10 to obtain a relation between the electromagnetic form factor for ^{4}He, $F^\gamma(Q^2)$, and the neutral weak form factor $F^Z(Q^2)$:

$$F^Z(Q^2) = -F^\gamma(Q^2)\left(4\sin^2\theta_W + \frac{2G_E^s}{G_E^{\gamma,p} + G_E^{\gamma,n}}\right), \qquad 29.$$

which then yields the parity-violating asymmetry for elastic e–^{4}He scattering:

$$A_{PV}^{\mathrm{He}} = \frac{G_F Q^2}{4\pi\sqrt{2}\alpha}\left(4\sin^2\theta_W + \frac{2G_E^s}{G_E^p + G_E^n}\right). \qquad 30.$$

One should keep in mind that radiative corrections, as discussed in Sections 3.1 and 3.2, lead to minor modifications of Equations 23 and 30 and must be included for any quantitative analysis.

Finally, we mention that quasi-elastic scattering from deuterium has been employed to study the axial form factor G_A^e. As mentioned above, doing so is not useful for constraining G_A^s but does provide a method to test the calculations of the radiative corrections and anapole contributions to G_A^e. In the static approximation, one can treat quasi-elastic scattering from deuterium as simply the sum of scattering from a free proton and a free neutron. In this case, the parity-violating asymmetry has the form

$$A_d = -\frac{G_F Q^2}{4\sqrt{2}\pi\alpha}\frac{\mathcal{N}_n + \mathcal{N}_p}{\mathcal{D}_n + \mathcal{D}_p}, \qquad 31.$$

where $\mathcal{N}_p$ ($\mathcal{D}_p$) and $\mathcal{N}_n$ ($\mathcal{D}_n$) are the numerators (denominators) in Equation 23 for the proton and the neutron, respectively. Again, the asymmetry can be expressed as a sum of three terms, $A_E + A_M + A_A$, which correspond to numerator expressions involving electric, magnetic, and axial weak form factors, respectively. At backward angles, the contribution of A_E is negligible. The strange magnetic form factor contribution to A_M is reduced because of the combination $(G_M^{\gamma,p} + G_M^{\gamma,n})G_M^s$ and the small value of the nucleon isoscalar magnetic form factor, relative to the axial term A_A. Thus, at backward angles the deuteron asymmetry, when combined with the proton asymmetry, can provide useful information about the isovector part of the weak axial form factor G_A^e. Again, it is important to include radiative corrections in any quantitative analysis. In addition, the nuclear effects associated with the binding of the two nucleons in deuterium must also be considered.

4.2. Experimental Technique

The need to precisely measure parity-violating asymmetries of the scale of a few parts per million (ppm) imposes several significant experimental challenges. High statistical precision demands a long running time and high luminosity, and hence high beam current and thick targets, as well as a highly polarized beam. The beam polarization must be well determined, which requires high-quality beam polarimetry. Backgrounds need to be well separated from the elastic or quasi-elastic scattering events of interest, and one must precisely correct for any residual background contributions. The beam helicity needs to be rapidly flipped (typically at approximately 30 Hz) to suppress the effect of slow changes in detector or beam properties. In the ideal case, no other beam property should change when the helicity is reversed. Fluctuations in beam properties such

as intensity, trajectory, and energy that are correlated with the helicity "flip" must be minimized, and the sensitivity of the apparatus to such helicity-correlated changes needs to be determined so that corrections can be made for the residual fluctuations. Additional slow flips of the beam helicity can then be made to suppress many remaining systematics. In this section, we discuss several aspects of the various approaches that have been adopted to meet these challenges.

4.2.1. Polarized electron source. The need for a highly polarized, high-current electron beam with exquisite stability under helicity reversal makes the polarized electron source a key component of these experiments. The adopted technology, pioneered at SLAC in the 1970s (17), is based on the emission of electrons from a GaAs photocathode when exposed to circularly polarized laser light. Beam polarizations of nearly 40% and currents of up to 100 μA were obtained through the use of "bulk" GaAs crystals for the photocathode (18). Higher polarization (at the expense of high beam current) was subsequently produced through the use of "strained" crystals, in which the active layer of the photocathode was a thin (∼100-nm) layer of GaAs grown on GaAsP (19). The mismatch between the two lattices produced a strain in the GaAs, breaking the degeneracy in its energy levels, which theoretically allowed a polarization of up to 100% (20, 21). More recently, the adoption of multilayer "superlattice" crystals (22) has enabled both high polarization (89%) and high current (100 μA) (23).

4.2.2. Beam monitoring and control. High-precision parity-violation experiments impose stringent requirements on the polarized electron beam in order to minimize false asymmetries generated by helicity-correlated variations in beam properties. These requirements demand careful attention to the optical properties of the incident laser light at the electron source.

Fast helicity reversal of the electron beam is accomplished by reversing the handedness of the laser light by use of a Pockels cell, which is a birefringent crystal whose indices of refraction change with the application of an electric field. Linearly polarized light from the source laser, with polarization at 45° to the transmission axes, acquires a phase shift between the components on the slow and fast axes; by adjusting the voltage, one can convert the light to either right- or left-handed circular polarization. Imperfections in the Pockels cell typically cause a small residual component of linear polarization, which differs for the two nominal circular polarization states. The linear components are transported differently by the various optical elements, leading to helicity-correlated intensity variations. Gradients in the birefringence in the cell also generate helicity-correlated changes in the trajectory of the light, which lead to electron-beam position variations (24) that, in turn, can also lead to intensity variations, given that the quantum efficiency of the photocathode usually varies over its surface. The adoption of strained GaAs photocathodes makes these effects especially acute: The strain introduces an anisotropy in the quantum efficiency of the cathode, making it the dominant source of analyzing power in the system.

Various passive and active techniques have been adopted to suppress these helicity-correlated effects. Passive techniques include careful alignment of the laser beam through the Pockels cell (25), minimization of optically active elements in the laser path, and attention to optimum beam transport in the accelerator to realize the natural "adiabatic damping" of position fluctuations in the acceleration process. Active techniques include feedback based on measurements of the helicity-correlated changes in beam intensity and position in the experimental hall.

Figure 4 depicts a typical polarized electron source setup, in this case the Thomas Jefferson National Accelerator Facility (Jefferson Lab) source as used in recent parity experiments (26–30). Two independent systems have been used to suppress the intensity variations. The first system uses adjustment of the voltage signal to the Pockels cell: Small differences in the voltages for the two helicity states modify the residual linear polarization of the transported light, leading to

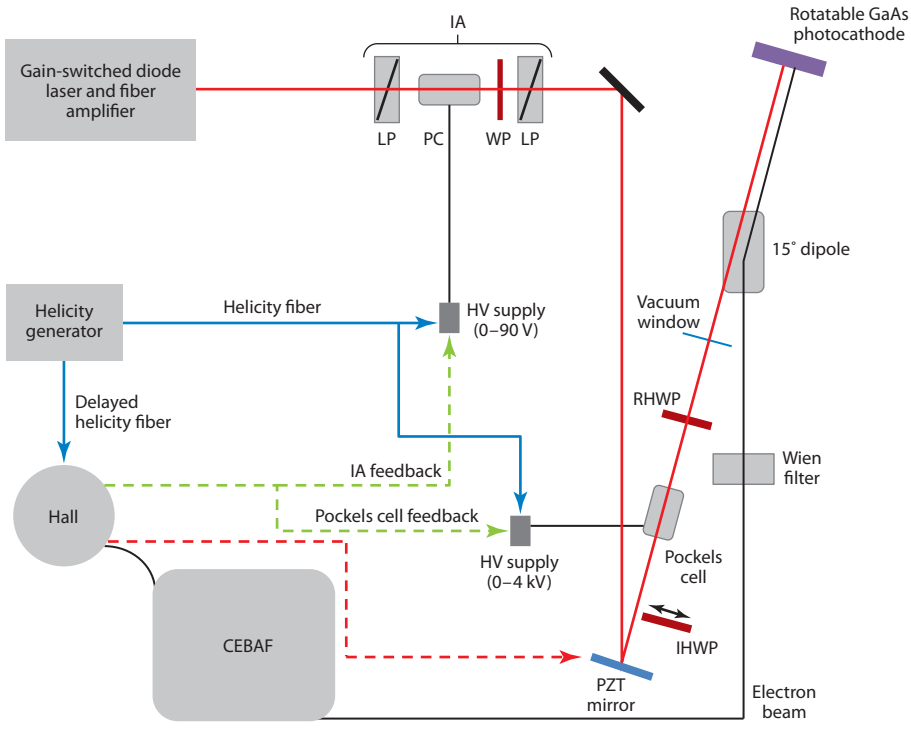

Figure 4

Schematic of the polarized injector source at Jefferson Lab. The laser light passes through an intensity attenuator system (IA) and is directed by a piezoelectric-controlled mirror (PZT) to the primary helicity-control Pockels cell. An insertable half–wave plate (IHWP) can be placed in the optical path. Passing through a rotatable half–wave plate (RHWP), the light is directed onto the photocathode. The emitted electron beam passes through a Wien filter to adjust the spatial orientation of the electron spin and is injected into the CEBAF accelerator. The helicity-generator signal is sent via fiber optics to both the high-voltage source for the Pockels cell and the experimental data-acquisition system. Helicity-correlated variations in the beam intensity and position are monitored in the experimental hall and can generate feedback signals to the source. Abbreviations: LP, linear polarizer; WP, wave plate.

helicity-correlated intensity variations that then can be adjusted. The second system, the intensity attenuator, consists of a second Pockels cell and a wave plate, sandwiched between two parallel linear polarizers. This Pockels cell is operated at low helicity-dependent voltages (to minimize beam-steering effects) and acts as an electro-optic adjustable shutter. In either case, helicity-correlated electron-beam intensity variations are measured, typically every few minutes, and a feedback signal is sent to the electron source to nullify the variations.

Both the SAMPLE experiment and the forward-angle phase of the G0 experiment also used active feedback on helicity-correlated position differences in the beam (31). Here, a piezoelectric-controlled steering mirror (**Figure 4**) is used to move the beam in a helicity-controlled manner.

Another technique is to use an insertable half–wave plate (IHWP) in the optical path (**Figure 4**). The IHWP is periodically inserted or removed on a timescale of many hours. The IHWP rotates the linear polarization state by 90°, thereby inverting the sense of the resulting circular polarization with respect to the Pockels cell voltage. This slow flip should reverse the sign of the measured asymmetry in the experimental hall with respect to the helicity-control signal, in the absence of any false asymmetry picked up in the experimental electronics due to that signal. Many sources

of helicity-correlated beam changes are insensitive to the state of the IHWP, so this flip cancels these systematics.

To ensure that there are no false asymmetries in the data due to the helicity-control signal being picked up by the experimental electronics, the fast helicity reversal follows a pseudorandom pattern, and the helicity state reported to the electronics is delayed by several states in the pattern and only later reconstructed by software. To illustrate the high suppression of helicity-correlated beam fluctuations afforded by these techniques, consider the HAPPEX-II experiment. The values of these variations, averaged over the entire several-month-long run, were 0.4 ppm for intensity, <1.7 nm for position, <0.2 nrad for the angle, and 0.2 ppb for energy. The sensitivity of the apparatus to these residual fluctuations can be determined either by performing a multiparameter linear regression of the natural fluctuations or by taking subsets of the data with individual beam parameters modulated in a controlled manner (50).

4.2.3. Beam polarimetry. Precise knowledge of the beam polarization is essential for normalizing the measured asymmetries. Experiments have adopted various polarimeters, including (*a*) those that measure continuously during the experiment, such as transmission (32, 33) and back-scattering (34–38) Compton polarimeters, and (*b*) those that are invasive and can make only periodic measurements of the polarization, such as Mott (39) and Møller (33, 40–42) polarimeters. The highest precision reached to date was achieved in the HAPPEX-III experiment, in which a combination of Møller and back-scattering Compton devices yielded a precision of 0.75% (23).

4.2.4. Counting versus integrating methods for asymmetry measurements. Two approaches have been adopted for measurements of the parity-violating asymmetry. The challenge is to accommodate the extremely high rates (of order 10 to 100 MHz) of scattered electrons that must be detected to achieve the desired statistical precision. The first approach is a counting method, in which custom electronics are used to collect events in scalars (the G0 experiment) or energy histograms (the PVA4 experiment), which are accumulated for a given beam helicity state and then digitized at each helicity transition. The second approach is the integrating method (the SAMPLE and HAPPEX experiments), in which the analog signal from the detectors is integrated over a given helicity window and the integral is digitized at each helicity change. Challenges in the counting method include accounting for the effects of electronic dead time and event pileup, which can distort the measured asymmetry, and optimizing the design and cost of the custom electronics. In the integrating method, one has to ensure a high degree of linearity of the entire electronics chain so that the helicity-correlated variations in the beam intensity do not generate false asymmetries. In neither approach, as opposed to typical nuclear physics experiments, can one digitize complete information about individual scattering events. Therefore, only limited off-line analysis techniques for dealing with background processes are available.

4.2.5. Targets. The program of parity-violating electron scattering experiments reviewed here generally involves the use of hydrogen, deuterium, and helium targets. The very small asymmetries to be measured require high luminosity, so these targets must be cryogenic to achieve sufficient areal density. The use of cryogenic fluids introduces a new challenge: ensuring the stability of the target density in the presence of the intense electron beam, which causes thermal heating of the fluid. Thermal fluctuations are a potential source of additional noise that can degrade the statistical precision of the asymmetry measurement.

4.2.6. Hydrogen and deuterium targets. The operating point of a liquid hydrogen target is typically ~19 K, only a few degrees below the boiling point at a nominal pressure of 1 to 2 atm.

Thus, even with small temperature excursions, the liquid remains significantly below the boiling point so as to minimize thermal fluctuations due to the beam. Indeed, localized boiling, leading to bubble formation, is a major potential source of target thickness variations that can contribute significantly to statistical noise in the measured asymmetries. The fluid is generally pumped in a recirculation loop to constantly provide fresh liquid within the electron-beam profile. The recirculation loop also contains a heat exchanger, in which heat is transferred to helium gas used as the primary coolant. An ohmic heater in the loop is used to control the temperature and maintain the operating point by compensating for variations in the beam power. Safety is a major consideration in the design and operation of these targets, given that the release of hydrogen gas into the room's atmosphere can lead to a dangerous flammable mixture. Detailed descriptions of the SAMPLE (43), G0 (44), and PVA4 (45) targets are available in the literature.

4.2.7. Helium targets. One experiment, HAPPEX-He, adopted a high-pressure ^{4}He gas target to directly measure the strange electric form factor G_E^s. The target was a 20-cm-long cell maintained at a temperature of 7 K and a pressure of 13 atm. The cryogenic ^{4}He was pumped through the cell in a direction transverse to the beam direction so as to minimize local beam heating. Even without the possibility of bubble formation, beam-induced density fluctuations in the gas posed a challenge, but they were limited to a few-percent increase in the statistical noise of the asymmetry measurement.

5. EXPERIMENTAL RESULTS

5.1. SAMPLE

The SAMPLE experiment, performed at the MIT–Bates Linear Accelerator Center, was focused primarily on determining the strange magnetic form factor G_M^s at low momentum transfer, $Q^2 = 0.1$ GeV^2. A rather complete description of the experiment and results can be found in Reference 33, and we provide a short summary here. A 200-MeV polarized electron beam, typically 40 μA, was incident on a 40-cm-long liquid hydrogen target. **Figure 5** shows a schematic of this apparatus. The scattered electrons were detected in a large–solid angle (∼1.5-sr) air Cherenkov

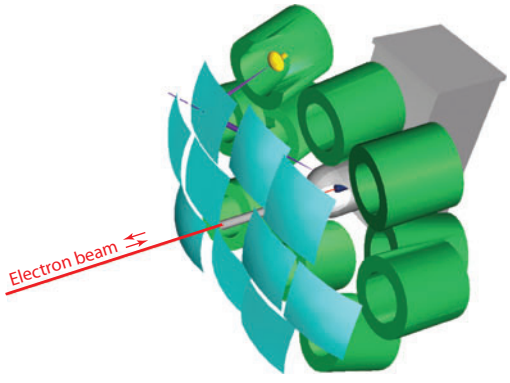

Figure 5

The geometry of the SAMPLE target and detector system. The electron beam is incident from the left. The electrons that were scattered at backward angles emitted Cherenkov light in the air, which was reflected by 10 mirrors onto 10 8-inch photomultiplier tubes. The photomultipliers were mounted inside cylindrical cast-lead shields to reduce background. Adapted from Reference 33 with permission.

detector that contained 10 ellipsoidal mirrors at backward angles ranging from 130° to 170°, which yielded an average Q^2 of approximately 0.1 $(\mathrm{GeV}/c)^2$. At these kinematics, the axial term was expected to contribute approximately 20% of the asymmetry.

The hydrogen data set was acquired in 1998, and the experiment was run with a deuterium target in 1999 to acquire data on the axial form factor. The initial deuterium result indicated a substantial discrepancy with calculations of the axial form factor, so further deuterium experiments at lower momentum transfer were performed in 2000 and 2001. These experiments, along with a reanalysis of the 1999 deuteron data set (with improved accounting of pionic backgrounds), have confirmed the theoretical treatment of the axial form factor.

The polarized electron source utilized bulk GaAs; the polarization was typically ~35%. The Bates beam was pulsed at 600 Hz, and the beam helicity was changed for each pulse. A preselected random pattern of 10 helicity states was generated, and the complement of this set (with reverse helicity) followed for the next 10 pulses. The longitudinal spin emerging from the polarized source was prerotated by a Wien spin rotator prior to injection into the accelerator, so the 36.5° magnetic bend into the experimental hall then provided longitudinal polarization at the target location. The beam polarization was periodically measured with a Møller polarimeter.

Each detector signal was integrated over the ~25 μs of the beam pulse and digitized, along with the beam charge for that pulse. The ratio of the integrated detector signal to the integrated beam charge (normalized yield) was then corrected for background, beam polarization, and other systematic beam effects to give the experimental result for the parity-violating asymmetry.

For the SAMPLE kinematics, the parity-violating asymmetry for elastic scattering on the proton for the incident electron energy of 200 MeV can be written as

$$A_p = -5.56 + 1.54 G_A^e(T = 1) + 3.37 G_M^s \text{ ppm}. \quad 32.$$

[The isoscalar component of G_A^e is computed to be very small (16), and we have absorbed it into the leading constant term.] The SAMPLE measurement of this asymmetry (46) is

$$A_p = -5.61 \pm 0.67_{\text{stat}} \pm 0.88_{\text{syst}} \text{ ppm}. \quad 33.$$

Use of the value of $G_A^e(T = 1) = -0.83 \pm 0.26$ from Reference 16 results in the strange magnetic form factor

$$G_M^s(Q^2 = 0.1) = 0.37 \pm 0.20 \pm 0.26 \pm 0.07, \quad 34.$$

where the first uncertainty is statistical, the second is the estimated experimental systematic uncertainty, and the last uncertainty is due to the axial corrections and electromagnetic form factors.

The asymmetry for quasi-elastic electron scattering deuterium for the SAMPLE kinematics and detector acceptance at 200 MeV is written

$$A_d = -7.06 + 1.66 G_A^e(T = 1) + 0.72 G_M^s \text{ ppm}, \quad 35.$$

where the corrections for deuteron structure and other nuclear effects, including hadronic parity violation, have been included as discussed in Reference 47. Note that the deuteron asymmetry is more sensitive to the contribution from the isovector axial form factor $G_A^e(T = 1)$ than the proton asymmetry is (48). The updated SAMPLE result for the deuterium asymmetry in quasi-elastic kinematics is (49)

$$A_d = -6.79 \pm 0.64_{\text{stat}} \pm 0.55_{\text{syst}} \text{ ppm}. \quad 36.$$

A combined fit of the H and D data, assuming that $G_E^s = 0$, allows a separation of G_M^s and $G_A^{T=1}$ and yields

$$G_M^s = 0.23 \pm 0.36_{\text{stat}} \pm 0.40_{\text{syst}} \quad 37.$$

and

$$G_A^e(T=1) = -0.53 \pm 0.57_{\text{stat}} \pm 0.50_{\text{syst}}, \quad 38.$$

which agree well with the H result (Equation 34) and with the theoretical prediction (16) for $G_A^e(T=1)$.

5.2. HAPPEX

The HAPPEX series of experiments were run in Hall A at Jefferson Lab and made use of high-resolution spectrometers (HRS) (51) to focus elastically scattered particles onto a total absorption shower counter in each focal plane; the signals were integrated over the 33-ms helicity period. The HRS suppressed background from inelastic scattering and low-energy secondaries.

The first-generation HAPPEX experiment ran in 1998 and 1999 (18, 19, 50) at kinematics $\langle\theta_{\text{lab}}\rangle = 12.3°$ and $\langle Q^2\rangle = 0.477\ (\text{GeV}/c)^2$. These values corresponded to the smallest angle and largest energy possible with the Hall A HRS, which maximized the figure of merit for a first measurement.

In the 1998 run, the experiment used an $I = 100\ \mu$A beam with $P = 38\%$ polarization produced from a bulk GaAs crystal. In the 1999 run, HAPPEX-I became the first experiment to use a strained GaAs photocathode to measure a parity-violating asymmetry in fixed-target electron scattering. This development improved the figure of merit P^2I with $P = 70\%$ and $I = 35\ \mu$A (50).

During HAPPEX-I, the Hall A Compton polarimeter (34) was commissioned. It provided, for the first time, continuous monitoring of the electron-beam polarization with a total relative error from run to run of less than 2%. The Compton results were in good agreement with the Møller polarimeter in Hall A and a Mott polarimeter located in the 50-MeV region of the accelerator.

The HAPPEX-I physics asymmetry was

$$A = -15.05 \pm 0.98_{\text{stat}} \pm 0.56_{\text{syst}}\ \text{ppm}. \quad 39.$$

The precision of the result was sufficient to rule out several then-current theoretical estimates of strangeness effects at moderately high Q^2, where it was thought the effects might have been large (50).

Using this result, along with the calculated G_A^{Zp} and the known values of the proton and neutron form factors, the experimenters determined the linear combination of strange form factors

$$G_E^s + 0.392 G_M^s = 0.014 \pm 0.020 \pm 0.010, \quad 40.$$

where the first error is the total experimental error (statistical and systematic errors added in quadrature) and the second error arises from the "ordinary" electromagnetic form factors. A feature of the HAPPEX experiments is that they have negligible sensitivity to the axial form factors, whose effect is kinematically suppressed due to the very forward scattering angle.

The second-generation HAPPEX experiments, HAPPEX-II and HAPPEX-He, took data in 2004 and 2005 at a lower Q^2 of $\sim$0.1 GeV^2 (27–29). They utilized superconducting septa magnets to allow the HRS to detect elastically scattered electrons at a scattering angle of 6°. The measurement on the ^{4}He target yielded an asymmetry of

$$A_{\text{He}} = +6.40 \pm 0.23_{\text{stat}} \pm 0.12_{\text{syst}}\ \text{ppm}, \quad 41.$$

which tightly constrained the strange electric form factor to $G_E^s = 0.002 \pm 0.014 \pm 0.007$. The hydrogen data asymmetry,

$$A_p = -1.58 \pm 0.12_{\text{stat}} \pm 0.04_{\text{syst}}\ \text{ppm}, \quad 42.$$

determined the form factor combination

$$G_E^s + 0.09 G_M^s = 0.007 \pm 0.011_{\text{stat}} \pm 0.006_{\text{syst}}, \quad 43.$$

which, again, was consistent with zero.

Subsequently, the HAPPEX-III experiment returned to higher Q^2 (0.62 GeV^2) with a data-taking run in 2009 (52). This measurement was motivated by indications of significant strange form factor contributions at high Q^2 (>0.4 GeV^2) in results from the forward-angle phase of the G0 experiment (see Section 5.3). HAPPEX-III capitalized on advances in polarimetry, control of helicity-correlated beam fluctuations, and an improved figure of merit compared with those of HAPPEX-I, leading to a precision asymmetry measurement of

$$A_p = -23.80 \pm 0.78_{\text{stat}} \pm 0.36_{\text{syst}} \text{ ppm}. \quad 44.$$

This measurement yielded the form factor combination

$$G_E^s + 0.517 G_M^s = 0.003 \pm 0.004_{\text{stat}} \pm 0.009_{\text{syst}}, \quad 45.$$

where the third error is due to electromagnetic form factors and radiative corrections. Again, the result is consistent with a net strangeness contribution of zero.

5.3. G0

The G0 experiment was performed in Hall C at Jefferson Lab. In this experiment, the parity-violating asymmetry in elastic electron scattering from hydrogen and quasi-elastic electron scattering from deuterium was measured in the Q^2 range from 0.1 to 1 (GeV/c)^2 in both forward- and backward-angle modes. By measuring three independent asymmetries, one at forward angles on liquid hydrogen and two at backward angles, where one was on liquid hydrogen and one on liquid deuterium, the experimenters achieved a complete separation of the strange vector form factors of the nucleon (G_M^s, G_E^s) and the isovector axial form factor [$G_A^e(T = 1)$]. In the forward-angle mode, the particle detected was the recoil proton, whereas in the backward-angle mode, the particle detected was the scattered electron. The experiment ran in forward-angle mode from 2002 through 2005 (26) and in backward-angle mode from 2006 through 2007 (30).

The G0 experiment employed a large-acceptance superconducting toroidal spectrometer with eight coils and eight sets of particle detectors, which provided excellent azimuthal symmetry about the beam axis. In forward-angle mode, the recoiling protons were detected with 16 pairs of plastic scintillation detectors in each octant. Each detector pair (one behind the other) selected coincident events to reduce accidental backgrounds. The incident beam of 3-GeV electrons was delivered in short (~100-ps) pulses at 31 MHz to allow a 32-ns time-of-flight window for detection of the recoil protons. Custom time-encoding electronics enabled measurement of the protons as a function of time of flight in pulse-counting mode. At the larger Q^2 of ≥ 0.3 (GeV/c)^2, large positive asymmetries due to hyperon decay backgrounds necessitated careful treatment and correction to extract the much smaller negative asymmetries arising from parity violation in elastic scattering. The forward-angle G0 measurements (26) enabled simultaneous determination of the quantity $G_E^s + \eta G_M^s$ over the Q^2 range between 0.1 and 1 (GeV/c)^2, where $\eta \equiv \tau G_M^\gamma / \varepsilon G_E^\gamma$. **Figure 6** shows the results.

The G0 backward-angle results were obtained through the use of incident beams at 359 MeV and 684 MeV. The orientation of the toroidal spectrometer was reversed to facilitate measurement of scattered electrons near 110° with respect to the incident beam direction. The scintillation detectors (known as focal plane detectors) were supplemented with additional scintillators (cryostat exit detectors) near the exit of the magnet and aerogel threshold Cherenkov counters (pion

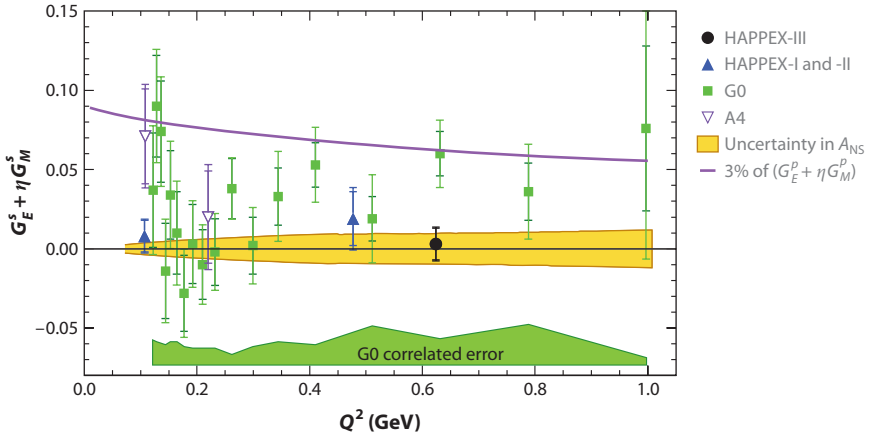

Figure 6

Strange quark vector form factor results from all forward-angle scattering measurements on the proton as a function of Q^2. For the G0 results (26), the inner error bars are statistical, and the outer error bars are point-to-point systematics; the correlated systematic error is shown as a green band. The yellow band shows the uncertainty in the predicted asymmetries in the absence of strangeness effects (A_{NS}), which arises from knowledge of the electromagnetic and axial form factors. For reference, the solid curve shows a 3% contribution to the comparable linear combination of proton form factors. Adapted from Reference 52 with permission.

threshold, 570 MeV) to reject pions. The backward-angle results (for hydrogen and deuterium) were combined with the forward-angle measurements to yield values of G_E^s, G_M^s, and G_A^e $(T = 1)$ (30) at two values of Q^2 (0.221 and 0.628 GeV^2) (**Figure 7**).

5.4. PVA4

The PVA4 Collaboration at the Mainz Microtron (MAMI) adopted a counting-mode approach that employs a highly segmented calorimeter along with custom fast electronics (**Figure 8**). No magnetic spectrometer is used; the signal is separated from backgrounds by use of the energy deposition in the calorimeter. The calorimeter is an azimuthally symmetric array of 1,022 PbF_2 crystals in seven rings covering scattered electron angles from either 30° to 40° (forward configuration) or 140° to 150° (backward configuration); it acts as a total-absorption Cherenkov detector (53). The spectrum of energy deposited above a hardware threshold in clusters of nine crystals is histogrammed using a pipelined fast digitizer, and the energy histograms are stored for each helicity state. The beam current is typically 20 μA with a polarization of 80%, and the helicity state is selected every 20 ms.

The first PVA4 measurement was in a forward-angle configuration with a liquid hydrogen target; the measured asymmetry was sensitive to a linear combination of G_E^s and G_M^s. The beam energy was 855 MeV, which yielded $Q^2 = 0.230$ (GeV/c)^2. For this initial measurement, only half of the 1,022 detector channels were instrumented. The measured asymmetry was (54)

$$A_p(Q^2 = 0.230) = -5.44 \pm 0.54_{\text{stat}} \pm 0.26_{\text{syst}} \text{ ppm}. \quad 46.$$

This asymmetry implies a value for the linear combination of the strange form factors of

$$(G_E^s + 0.225 G_M^s)(Q^2 = 0.230) = 0.039 \pm 0.034. \quad 47.$$

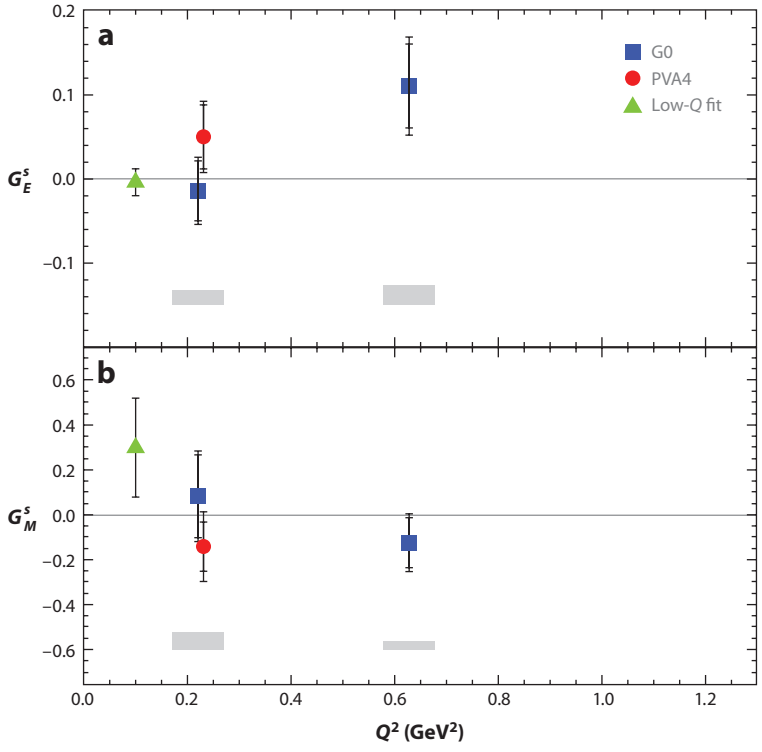

Figure 7

(*a*) Results for the strange vector form factors extracted by combining the forward- and backward-angle G0 experiments on hydrogen and deuterium (30). (*b*) Also shown are the results from PVA4 at $Q^2 = 0.23$ GeV^2 (54, 56), and a global fit (58) to world data at $Q^2 = 0.1$ GeV^2. The gray bands are correlated systematic errors for the G0 data. Adapted from Reference 30 with permission.

The second PVA4 forward-angle measurement made use of the fully instrumented detector. Data were taken on liquid hydrogen with a beam energy of 570 MeV at $Q^2 = 0.108$ (GeV/c)^2 and yielded an asymmetry of

$$A_p(Q^2 = 0.108) = -1.36 \pm 0.29_{\text{stat}} \pm 0.13_{\text{syst}} \text{ ppm}, \qquad 48.$$

which implies the value of

$$\left(G_E^s + 0.106 G_M^s\right)(Q^2 = 0.108) = 0.071 \pm 0.036 \qquad 49.$$

for the linear combination (55). The latter result represents a nearly 2-σ deviation from zero.

Following these two forward-angle measurements, the PVA4 apparatus was turned around and modified for a series of backward-angle measurements. Added to the detector was a double-ring of 72 scintillator counters, each of which covers 14 of the PbF_2 detectors. These detectors are used for electron tagging to suppress the copious background of photons arising from π^0 decay.

The first backward-angle measurement on hydrogen was at a 315-MeV beam energy and a Q^2 of 0.230 (GeV/c)^2 to match the Q^2 of one of the forward-angle points. The result was (56)

$$A_p(Q^2 = 0.230) = -17.23 \pm 0.82_{\text{stat}} \pm 0.89_{\text{syst}} \text{ ppm}. \qquad 50.$$

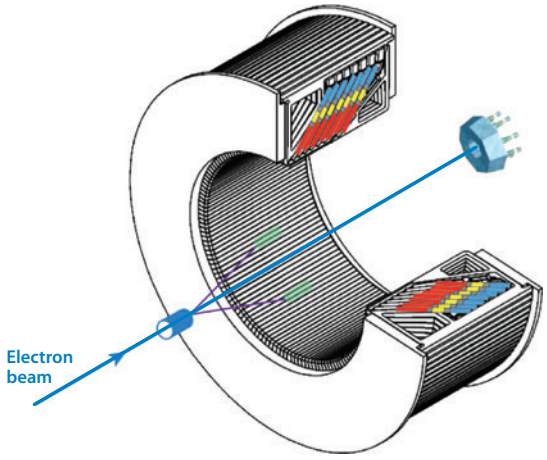

Figure 8

Layout of the PVA4 detector. The electron beam is incident from the left; scattered electrons are detected in the projective-geometry PbF_2 calorimeter, which consists of 7 rings of crystals in 146 rows. Beam intensity fluctuations are monitored with a water Cherenkov luminosity monitor system that detects small-angle scattering (*right*).

The measured asymmetry implies a value for the linear combination of the strange form factors of

$$(G_M^s + 0.26G_E^s)\,(Q^2 = 0.230) = -0.12 \pm 0.11_{\text{stat}} \pm 0.11_{\text{syst}}. \qquad 51.$$

Data were also taken at the same kinematics with a liquid deuterium target; results are expected soon (57). The MAMI accelerator has undergone an energy upgrade to provide beam energies up to 1.5 GeV, which will open up a wider range of Q^2 for the PVA4 experiment. The collaboration has since moved the detector back into its forward scattering configuration (57) and has taken data at $Q^2 = 0.63$ $(\text{GeV}/c)^2$, which matches the kinematics of both the HAPPEX-III experiment and the higher-Q^2 point at backward angles from G0.

6. CONCLUSIONS

During the past decade, there has been a substantial international effort to perform measurements of parity-violating asymmetries in elastic electron scattering from nucleons. The primary aim of this program has been to constrain the strange quark–antiquark contributions to the nucleon electroweak form factors, G_E^s and G_M^s, as a function of momentum transfer Q^2. The experiments have made great progress in advancing the techniques required to perform reliable and precise measurements that enable extraction of the form factors. Substantial theoretical effort has provided confidence in the radiative corrections and the degree of uncertainty associated with contributions to the axial form factor G_A^e. As a result, a clear picture has emerged from this body of work.

In general, a convincing signal for a significant strange quark–antiquark effect in the vector form factors has not been obtained from these measurements. All the various experimental results at different kinematics seem to support this general conclusion. In fact, the results are remarkably consistent with this conclusion, despite the difficulty of these challenging experiments.

At the lowest momentum transfers [$Q^2 \sim 0.1$ $(\text{GeV}/c)^2$], global fits have been performed to the body of experimental data in this kinematic region (58, 59). These fits illustrate the consistency

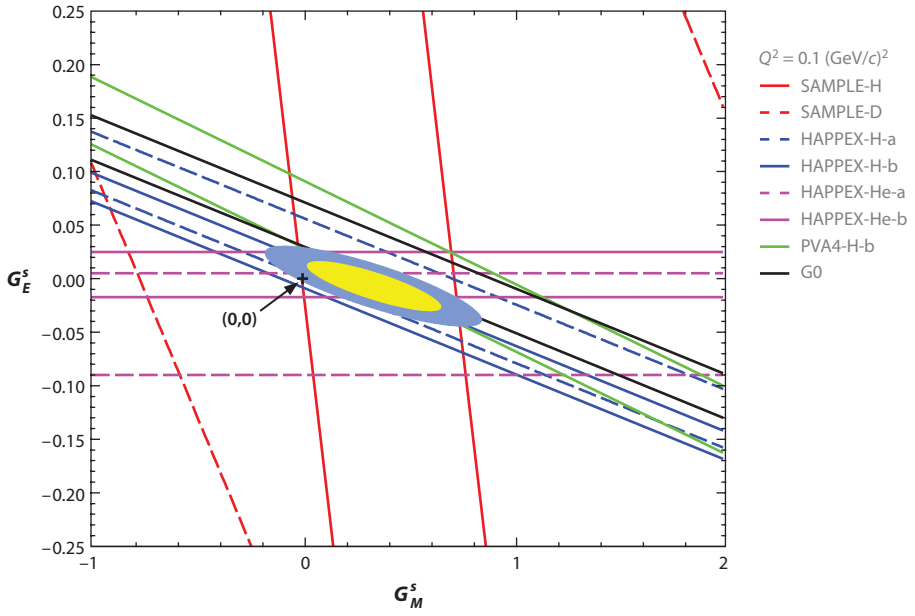

Figure 9

The world data constraints on (G_E^s, G_M^s) at $Q^2 = 0.1$ (GeV/c)^2 (58). The form factors from Reference 60 are used. Different bands in the plot represent SAMPLE-H (*solid red*) (46), SAMPLE-D (*dashed red*) (49), HAPPEX-H-a (*dashed blue*) (27), HAPPEX-H-b (*solid blue*) (29), HAPPEX-He-a (*dashed pink*) (28), HAPPEX-He-b (*solid pink*) (29), PVA4-H-b (*solid green*) (55), and the three lowest-Q^2 bins in the G0 forward angle (*solid black*) (26). The yellow and blue ellipses represent 68.27% ($\Delta\chi^2 = 2.3$)- and 95% ($\Delta\chi^2 = 5.99$)-confidence contours around the point of maximum likelihood at ($G_E^s = 0.006$, $G_M^s = 0.33$). The black cross represents $G_E^s = G_M^s = 0$. Reprinted from Reference 58 with permission.

of the data and reinforce the conclusion that the strange vector form factors are small (compared with many model predictions) at this low Q^2. **Figure 9** shows the result of the most recent global fit (58). As a result, one can now conclude, with 95% confidence, that strange quarks contribute less than 5% of the mean-square charge radius and less than 6% of the magnetic moment of the proton.

These results are surprising in light of the guidance from many models of nucleon structure that predicted substantial strange quark effects at low Q^2. The result also seems to be at variance with the notion that baryon-meson fluctuations are a significant aspect of nucleon structure, as one would infer from the $\bar{d} - \bar{u}$ asymmetry observed in Drell–Yan production and the success of many meson cloud models of the nucleon. More recent results based on lattice QCD calculations (7–9) seem to support the very small values of the strange form factors indicated by the experiments. It is certainly gratifying that these calculations are consistent with experimental results. Nevertheless, they do not provide much insight into why the strange quark contributions are suppressed in these quantities. Ultimately, we must admit that we have learned something significant about nucleon structure from this program but that a deeper understanding of this phenomenon is still lacking.

On the practical side, the conclusion that strange form factors are constrained to be small, combined with the development of experimental techniques for parity-violating electron scattering experiments, has motivated new experiments to perform precision tests of the standard electroweak model in parity-violating electron scattering. In particular, the experimental program reviewed here, and the constraint on the strange electric form factor of the proton G_E^s, provides a quantitative

basis for assessing the utility of low-Q^2 measurements of parity-violating electron scattering to provide precise new information on the running of the weak mixing angle θ_W (61). For example, the QWeak experiment at Jefferson Lab (62, 63) is under way and expects to provide a measurement of $\sin^2 \theta_W$ to a precision of approximately 0.24%. Such a measurement would herald a new era of precision tests of the Standard Model that could reveal effects associated with new physics at the TeV scale.

DISCLOSURE STATEMENT

The authors are not aware of any affiliations, memberships, funding, or financial holdings that might be perceived as affecting the objectivity of this review.

ACKNOWLEDGMENTS

This work was supported in part by US Department of Energy contract DE-AC05-06OR23177, under which Jefferson Science Associates, LLC, operates the Thomas Jefferson National Accelerator Facility, and by National Science Foundation grants PHY-0758068 and PHY-1068667. We also thank our colleagues in the SAMPLE, HAPPEX, G0, and PVA4 Collaborations for many fruitful discussions and interactions.

LITERATURE CITED

1. Kaplan D, Manohar A. *Nucl. Phys. B* 310:527 (1988)
2. McKeown RD. *Phys. Lett. B* 219:140 (1989)
3. Beck DH. *Phys. Rev. D* 39:3248 (1989)
4. Martin AD, Stirling WJ, Thorne RS, Watt G. *Eur. Phys. J. C* 63:189 (2009)
5. Nakamura K, et al. (Part. Data Group) *J. Phys. G* 37:075021 (2010)
6. Beck DH, Holstein BR. *Int. J. Mod. Phys. E* 10:1 (2001)
7. Leinweber DB, et al. *Phys. Rev. Lett.* 94:212001 (2005)
8. Leinweber DB, et al. *Phys. Rev. Lett.* 97:022001 (2006)
9. Doi T, et al. *Phys. Rev. D* 80:094503 (2009)
10. Erler J, Kurylov A, Ramsey-Musolf MJ. *Phys. Rev. D* 68:016006 (2003)
11. Erler J, Ramsey-Musolf MJ. *Phys. Rev. D* 72:073003 (2005)
12. Budd H, Bodek A, Arrington J. arXiv:hep-ex/0308005 (2003)
13. Filippone BW, Ji XD. *Adv. Nucl. Phys.* 26:1 (2001)
14. Adams D, et al. (Spin Muon Collab.) *Phys. Rev. D* 56:5330 (1997)
15. Zeldovich, Ya B. *J. Exp. Theor. Phys.* 6:1184 (1958)
16. Zhu S, et al. *Phys. Rev. D* 62:033008 (2000)
17. Prescott CY, et al. *Phys. Lett. B* 77:347 (1978)
18. Aniol KA, et al. *Phys. Rev. Lett.* 82:1096 (1999)
19. Aniol KA, et al. *Phys. Lett. B* 509:211 (2001)
20. Nakanishi T, et al. *Phys. Lett. A* 158:345 (1991)
21. Maruyama T, et al. *Phys. Rev. Lett.* 66:2376 (1991)
22. Maruyama T, et al. *Appl. Phys. Lett.* 85:2640 (2004)
23. Ahmed Z, et al. arXiv:1107.0913 (2011)
24. Humensky TB, et al. *Nucl. Instrum. Methods A* 521:261 (2004)
25. Paschke KD. *Eur. Phys. J. A* 32:549 (2007)
26. Armstrong DS, et al. *Phys. Rev. Lett.* 95:092001 (2005)
27. Aniol KA, et al. *Phys. Lett. B* 635:275 (2006)
28. Aniol KA, et al. *Phys. Rev. Lett.* 96:022003 (2006)

29. Acha A, et al. *Phys. Rev. Lett.* 98:032301 (2007)
30. Androic D, et al. *Phys. Rev. Lett.* 104:012001 (2010)
31. Averett T, Jones CS, McKeown RD, Pitt M. *Nucl. Instrum. Methods A* 438:246 (1999)
32. Weinrich C. *Eur. Phys. J. A* 24S2:129 (2005)
33. Beise EJ, Pitt ML, Spayde DT. 2005. *Prog. Part. Nucl. Phys.* 54:289 (2005)
34. Baylac M, et al. *Phys. Lett. B* 539:8 (2002)
35. Neyret D, et al. *Nucl. Instrum. Methods A* 443:231 (2000)
36. Jorda JP, et al. *Nucl. Instrum. Methods A* 412:1 (1998)
37. Falleto N, et al. *Nucl. Instrum. Methods A* 459:412 (2001)
38. Diefenbach J. *Hyperfine Int.* 200:41 (2011)
39. Price JS, et al. Presented at Int. Symp. High Energy Spin Phys., 13th, Protvino, Russ. (1998)
40. Glamazdin AV, et al. *Fizika B* 8:91 (1999)
41. Hauger M, et al. *Nucl. Instrum. Methods A* 462:382 (2001)
42. Bartsch P. PhD thesis, Inst. Kernphys., Univ. Mainz. 86 pp. (2002)
43. Beise E, et al. *Nucl. Instrum. Methods A* 378:383 (1996)
44. Covrig S, et al. *Nucl. Instrum. Methods A* 551:218 (2005)
45. Altarev I, et al. *Nucl. Instrum. Methods A* 640:58 (2006)
46. Spayde DT, et al. *Phys. Rev. Lett.* 84:1106 (2000)
47. Sciavilla R, Carlson J, Paris MW. *Phys. Rev. C* 70:044007 (2004)
48. Beise EJ, McKeown RD. *Nucl. Part. Phys.* 20:105 (1991)
49. Ito TM, et al. *Phys. Rev. Lett.* 92:102003 (2004)
50. Aniol KA, et al. *Phys. Rev. C* 59:065501 (2004)
51. Alcorn J, et al. *Nucl. Instrum. Methods A* 522:294 (2004)
52. Ahmed Z, et al. *Phys. Rev. Lett.* 108:102001 (2012)
53. Baunack S, et al. *Nucl. Instrum. Methods A* 640:58 (2011)
54. Maas FE, et al. *Phys. Rev. Lett.* 93:022002 (2004)
55. Maas FE, et al. *Phys. Rev. Lett.* 94:152001 (2005)
56. Baunack S, et al. *Phys. Rev. Lett.* 102:151803 (2009)
57. Baunack S. *Hyperfine Int.* 200:13 (2011)
58. Liu J, McKeown RD, Ramsey-Musolf MJ. *Phys. Rev. C* 76:025202 (2007)
59. Young RD, Roche J, Carlini RD, Thomas AW. *Phys. Rev. Lett.* 97:102002 (2006)
60. Kelly JJ. *Phys. Rev. C* 70:068202 (2004)
61. Young RD, Carlini RD, Thomas AW, Roche J. *Phys. Rev. Lett.* 99:122003 (2007)
62. Carlini RD, et al. arXiv:1202.1255 [physics-ins.det] (2012)
63. van Oers WTH. *Nucl. Phys. A* 805:329 (2008)

Annual Review of Nuclear and Particle Science

Volume 62, 2012

Contents

Indexes

Errata

An online log of corrections to *Annual Review of Nuclear and Particle Science* articles may be found at http://nucl.annualreviews.org/errata.shtml